Photocatalytic Degradation of Paracetamol under Simulated Sunlight by Four TiO2 Commercial Powders: An Insight into the Performance of Two Sub-Micrometric Anatase and

Original

Photocatalytic Degradation of Paracetamol under Simulated Sunlight by Four TiO2 Commercial Powders: An Insight into the Performance of Two Sub-Micrometric Anatase and Rutile Powders and a Nanometric Brookite Powder / Blangetti, N., Freyria, F.S., Chiara Calviello, M., Ditaranto, N., Guastella, S., Bonelli, B.. - In: CATALYSTS. - ISSN 2073-4344. - 13:2(2023). [10.3390/catal13020434]

Publisher:
MDPI

Published
DOI:10.3390/catal13020434

catalysts

MDPI

Article

Photocatalytic Degradation of Paracetamol under Simulated Sunlight by Four TiO_2 Commercial Powders: An Insight into the Performance of Two Sub-Micrometric Anatase and Rutile Powders and a Nanometric Brookite Powder

Nicola Blangetti [1], Francesca S. Freyria [1,*], Maria Chiara Calviello [1], Nicoletta Ditaranto [2], Salvatore Guastella [1] and Barbara Bonelli [1,3,*]

[1] Department of Applied Science and Technology and INSTM Unit of Torino-Politecnico, Corso Duca degli Abruzzi 24, I-10129 Torino, Italy
[2] Dipartimento di Chimica, Università degli Studi di Bari Aldo Moro, I-70125 Bari, Italy
[3] Interdepartmental Centre PolitoBIOMed Lab, Corso Duca degli Abruzzi 24, I-10129 Torino, Italy
* Correspondence: francesca.freyria@polito.it (F.S.F.); barbara.bonelli@polito.it (B.B.)

Abstract: The photocatalytic degradation of the emerging contaminant paracetamol in aqueous solution has been studied under 1 SUN (~1000 W m^{-2}) in the presence of four commercial TiO_2 powders, namely sub-micrometric anatase and rutile, and nanometric brookite and P25 (the popular anatase/rutile mixture used as a benchmark in most papers). The rutile powder showed low activity, whereas, interestingly, the anatase and the brookite powders outperformed P25 in terms of total paracetamol conversion to carboxylic acids, which, according to the literature, are the final products of its degradation. To explain such results, the physicochemical properties of the powders were studied by applying a multi-technique approach. Among the physicochemical properties usually affecting the photocatalytic performance of TiO_2, the presence of some surface impurities likely deriving from K_3PO_4 (used as crystallization agent) was found to significantly affect the percentage of paracetamol degradation obtained with the sub-micrometric anatase powder. To confirm the role of phosphate, a sample of anatase, obtained by a lab synthesis procedure and having a "clean" surface, was used as a control, though characterized by nanometric particles and higher surface area. The sample was less active than the commercial anatase, but it was more active after impregnation with K_3PO_4. Conversely, the presence of Cl at the surface of the rutile did not sizably affect the (overall poor) photocatalytic activity of the powder. The remarkable photocatalytic activity of the brookite nanometric powder was ascribed to a combination of several physicochemical properties, including its band structure and nanoparticles size.

Keywords: solar photocatalysis; advanced oxidation processes; paracetamol; TiO_2; emerging contaminants; water remediation

check for updates

Citation: Blangetti, N.; Freyria, F.S.; Calviello, M.C.; Ditaranto, N.; Guastella, S.; Bonelli, B. Photocatalytic Degradation of Paracetamol under Simulated Sunlight by Four TiO_2 Commercial Powders: An Insight into the Performance of Two Sub-Micrometric Anatase and Rutile Powders and a Nanometric Brookite Powder. *Catalysts* **2023**, *13*, 434. https://doi.org/10.3390/catal13020434

Academic Editors: Giuseppina Pinuccia Cerrato, Claudia Letizia Bianchi and Lorenzo Mino

Received: 12 January 2023
Revised: 9 February 2023
Accepted: 14 February 2023
Published: 17 February 2023

1. Introduction

Emerging contaminants, or more precisely "contaminants of emerging concern" [1], are substances of different origins and types (e.g., dyes, herbicides, pesticides, caffeine, drugs, and their metabolites, personal care products, etc.) that have been detected, not only in wastewater, but also in drinking water, surface water (even in protected nature conservation areas) [2], groundwater aquifers [3], and meltwater from three Alpine glaciers [4], thanks to the development of extremely sensitive analytical and sensing method [1,5–9]. Emerging contaminants, which can pose serious risks to both humans and the environment even at small concentrations, occur as micro-pollutants [3,10,11], i.e., in concentration from a few ng L^{-1} to several g L^{-1}, because current traditional treatments of urban water are unable to remove them. Some of their properties, e.g., high solubility in water with low adsorption in soil, leading to high mobility in the aquifer [12–14], make micro-pollutants kind of species that are difficult to immobilize and treat by traditional water treatment methods.

Among the different kinds of emerging pollutants identified so far, pharmaceutical products are of worldwide scientific concern due to their unpredictable impact on environmental equilibrium and possible toxic effects on ecosystems [7,15–17]. Though different countries have specific regulations concerning pharmaceutical production, administration, and usage, the continuous aging of the population, and improvement of life quality are leading to an increase in medicine consumption and, consequently, their occurrence in wastewater will keep increasing [10,18,19].

Nowadays, the effects of pollution by emerging contaminants, in particular pharmaceutical and personal care products (PPCPs), are not well understood, since they can induce mostly sub-lethal effects even at low dosages by affecting natural systems via direct or cascading effects [7,12,20]. An example of the PPCPs' effect on the natural system is their contribution to enhancing the antimicrobial resistance of microorganisms which is a matter of worldwide concern. Paracetamol (Scheme 1), also known as acetaminophen, N-acetyl-para-aminophenol, and Tylenol, is a common analgesic and antipyretic medication for mild-to-moderate pain and fever and is one of the most investigated drugs along with ibuprofen, diclofenac, naproxen, and ketoprofen. Being available in different forms (pills, effervescent tablets, suppositories, syrups, or injections) and generally without any medical prescription, it is widely consumed. Paracetamol is one of the most frequently detected compounds in secondary effluents among analgesics drugs [18] and appeared among one of the highest concentrations of the active pharmaceutical ingredients (APIs) detected in the analyses of 258 rivers spread all around the world with a detection frequency almost constant everywhere [21]. Moreover, during the COVID-19 pandemic, paracetamol was one of the most used self-medications [22]. For example, in Tyrol (Austria, EU) at the beginning of the pandemic, its consumption doubled passing from 8000 mg/day/1000 inhabitants to 12,000–14,000 mg/day/1000 inhabitants [23], generating a higher probability of its occurrence in wastewater, drinking water, and fresh waters, gaining the third position in the list of 3466 water micropollutants that deserve more global attention [10].

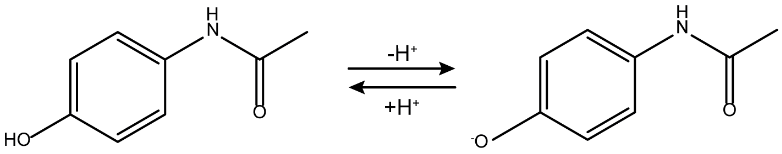

Scheme 1. Paracetamol (IUPAC name: N-(4-Hydroxyphenyl)acetamide) chemical structure and its dissociation equilibrium in water (pK_a = 9.5).

Already before the COVID-19 outbreak, in drinking water, for instance, in the U.S., 0.002 $\mu g\ L^{-1}$ paracetamol was detected in 7 % of the analyzed samples and up to 10 µg. L^{-1} in a nationwide reconnaissance [24]. A paracetamol concentration between 0.260 and 0.010 $\mu g\ L^{-1}$ was detected in Spain, and a concentration of 0.045 $\mu g\ L^{-1}$ in the Marseille area (France) [25]; 227 $\mu g\ L^{-1}$ paracetamol was detected in Rio Seke Bolivia, i.e., in freshwater [26], and other rivers all around the world [1,21].

For the aforementioned reasons, lowering the concentration of emerging pollutants is important and new strategies for water remediation should be developed [27]. With respect to non-reactive (conservative) methods, this implies the direct removal of the contaminant, with micro-pollutants the best results have been obtained, so far, by membranes technology i.e., by reverse osmosis or nanofiltration [28,29]; reactive methods include advanced oxidation processes (AOPs) based on the production of highly reactive radicals, or chemical species able to oxidize/reduce micro-pollutants may be used as stand-alone methods or coupled to other technologies [30–32]. AOPs consist of a wide range of operative settings based on efficient redox technologies that outperform some conventional treatments [13,33,34].

TiO_2 is one of the most promising semiconductors for the photocatalytic removal of environmental pollutants, as several organic molecules can be degraded to small fragments or undergo mineralization at ambient temperature and pressure in water [31,32]. The set of reactions recognized to occur when TiO_2 interacts with light is reported here:

$$TiO_2 + h\nu \rightarrow e^-_{CB} + h^+_{VB} \tag{1}$$
$$e^-_{CB} + O_2 + H^+ \rightarrow HO_2\cdot \tag{2}$$
$$e^-_{CB} + HO_2\cdot + H^+ \rightarrow H_2O_2 \tag{3}$$
$$2e^-_{CB} + O_2 + 2H^+ \rightarrow H_2O_2 \tag{4}$$
$$h^+_{VB} + H_2O \rightarrow HO\cdot + H^+ \tag{5}$$
$$2\ HO\cdot \rightarrow H_2O_2 \tag{6}$$
$$H_2O_2 + h\nu \rightarrow 2\ HO\cdot \tag{7}$$
$$H_2O_2 + e^-_{CB} + H^+ \rightarrow HO\cdot + H_2O \tag{8}$$

In summary, interaction with a light of energy larger than the bandgap of TiO_2 promotes electrons in the conduction band (CB, e^-_{CB}) and generates holes in its valence band (VB, h^+_{VB}). The photogenerated charge carriers then undergo a series of reactions producing radical species (e.g., $HO\cdot$). Two main factors decrease the photocatalyst efficiency, the recombination of the photogenerated e^-_{CB} and h^+_{VB}, and the bandgap of TiO_2, normally requiring UV light, which in turn represents a small fraction of the solar spectrum. Among AOPs methods, photocatalytic degradation [35] under solar light would be an important challenge with an undoubtedly environmental impact, and for this application, the use of commercially available photocatalysts could help spread this method. Simultaneously, other photocatalysts could be engineered based on the deep knowledge of the commercially available ones. Indeed, the photocatalytic activities of samples produced in different labs by different syntheses are sometimes hardly comparable, whereas commercial samples should be reliable and well-characterized to act, at least, as benchmarks, as it happens with Degussa P25, used in most catalytic studies [36,37].

Here, we aim at studying the degradation of the emerging pollutant paracetamol under simulated solar light (1 SUN) by using different commercial powders, namely one anatase, one rutile, one brookite sample, and Degussa P25, hereafter referred to as P25. Notoriously, the photocatalytic activity of TiO_2 is the result of several physicochemical properties. In addition to its bandgap energy, specific surface area, porosity, type of polymorphs phase(s), presence of heterojunctions (which can stabilize the photogenerated e^-_{CB} and h^+_{VB}) [36–38], the presence of Ti^{3+} species (i.e., self-doping), surface defects, and surface charge can contribute to the overall photocatalytic efficiency. These aspects were therefore considered during the powders' physicochemical characterization, along with the presence of chemical impurities, which can have a critical photocatalytic role, as well. For this reason, a sample of pure anatase has been obtained by a well-established lab synthesis procedure and used as a control, as it did not contain any surface impurities [38–41].

2. Results and Discussion

2.1. Physicochemical Characterization

Figure 1 reports the XRD patterns of the studied powder samples. As expected, the P25 sample shows the peaks of both anatase (A) and rutile (R). Furthermore, the peaks of anatase, the Comm_A powder shows a peak at 27.43 2θ value, assigned to the d_{110} most intense reflection of rutile (JCPDS file n° 01-071-0650), indicating the presence of this phase, at least in traces; the Comm_R sample shows a peak at 25.3 2θ value, assigned to the d_{101} reflection of anatase (JCPDS file n° 01-078-2486), indicating the presence of minor amounts of this phase, whereas the Comm_B sample only shows the peaks of brookite. Both Comm_A and Comm_R showed sharper XRD peaks, as compared to P25, Comm_B, and Lab_A. Accordingly, the crystallite size of the main phase, as determined by the Williamson-Hall method (Table 1), was larger with Comm_A and Comm_R samples. The Quantitative Phase Analysis (QPA), as carried out by Rietveld refinement, allowed quantifying the amounts of all the occurring phases (Table 1), showing the occurrence of some rutile (1.7 %) in Comm_A and anatase (4.6 %) in Comm_R; the phase composition of

P25 was 88 % anatase and 12 % rutile, whereas brookite and anatase were the only phases occurring in Comm_B and Lab_A, respectively.

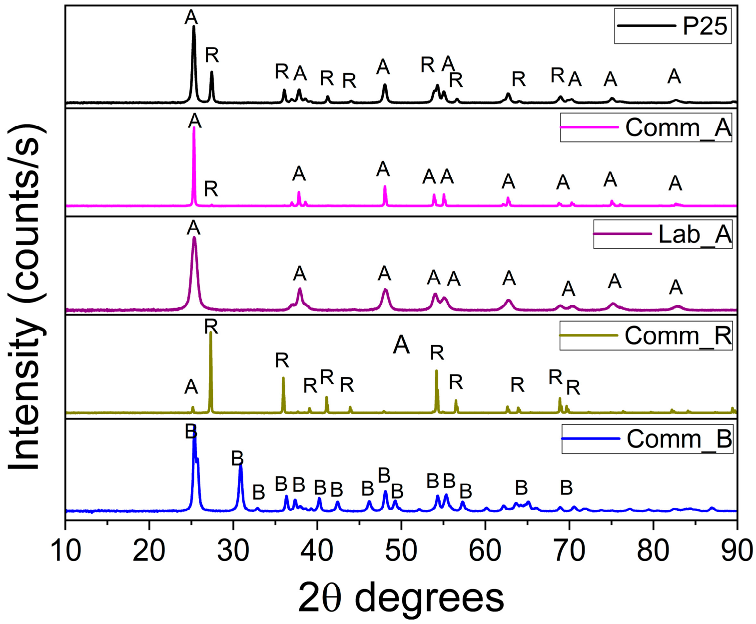

Figure 1. XRD patterns of the studied powder samples. The main peaks of anatase, rutile, and brookite are labeled as A, R, and B, respectively.

Table 1. Some relevant textural and surface properties of the studied powder samples as obtained by XRD followed by ^{a} Rietveld refinement, ^{b} N_2 isotherms at −196 °C, ^{c} EDX elemental analysis, ^{d} XPS elemental analysis, and ^{e} electrophoretic measurements.

Sample	**QPA (Phase wt.%)** ^{a}	**Crystallite Size, nm (±)** ^{a}	**BET SSA ($m^2\ g^{-1}$)** ^{b}	**V_{tot} ($cm^3\ g^{-1}$)** ^{b}	**EDX** ^{c} **Determined Impurities (at. %)**	**XPS** ^{d} **Determined Impurities (at. %)**	**pH_{IEP}** ^{e}
Comm_A	98.3 (A) 1.7 (R)	108.9 (0.9) 180.2 (31.7)	8.98	0.0300	K (0.16) P (0.27)	K (2.9) P (2.7)	1.31
Comm_R	4.6 (A) 95.4 (R)	119.5 (12.4) 209.6 (8.7)	2.65	0.00554	Not detected	Cl (0.7)	2.87
Comm_B	100 (B)	23 (0.7)	38.09	0.347	Cl (0.03)	Not detected	5.11
P25	88 (A) 12 (R)	19 (3) 23 (4)	51.21	0.188	Cl (0.09)	Not detected	6.77
Lab_A	100 (A)	12.4 (1.3)	150	0.280	Not detected	Not detected	6.07

A selected FESEM image of the Lab_A sample (Figure 2) shows the occurrence of nanoparticles with a rather uniform size of ca. 10 nm (of the order of the crystallite size reported in Table 1), in agreement with a previous study on a powder obtained by the same synthesis method, which allows obtaining single phase anatase nanoparticles of uniform shape and size [38,39]. The FESEM morphological analysis of the commercial powders shows that both Comm_A and Comm_R are characterized by larger (submicrometric) particles with heterogenous size. With the Comm_A sample, this was likely due to the adopted synthesis procedure, during which K_3PO_4 is often used as crystallization agent [42], whereas the Comm_R particle size is because rutile tends to form larger crystallites/particles [43]. Smaller (nanometric) particles occur in P25, forming agglomerates/aggregates, and small irregular nanoparticles also occur in Comm_B, confirming the occurrence of a nanometric powder (as reported by the producer) where nanoparticles form larger (orthorhombic) agglomerates/aggregates. With P25, Comm_R, and Comm_A, the crystallite size (as determined by XRD) is close to the particle size (as determined by FESEM); the larger error of the rutile crystallite size measured in Comm_A likely derives from the small abundance of such polymorph in the sample. Comparison between the crystallite size and the size of the nanoparticles in Comm_B is not straightforward, due to the peculiar nanoparticles' morphology.

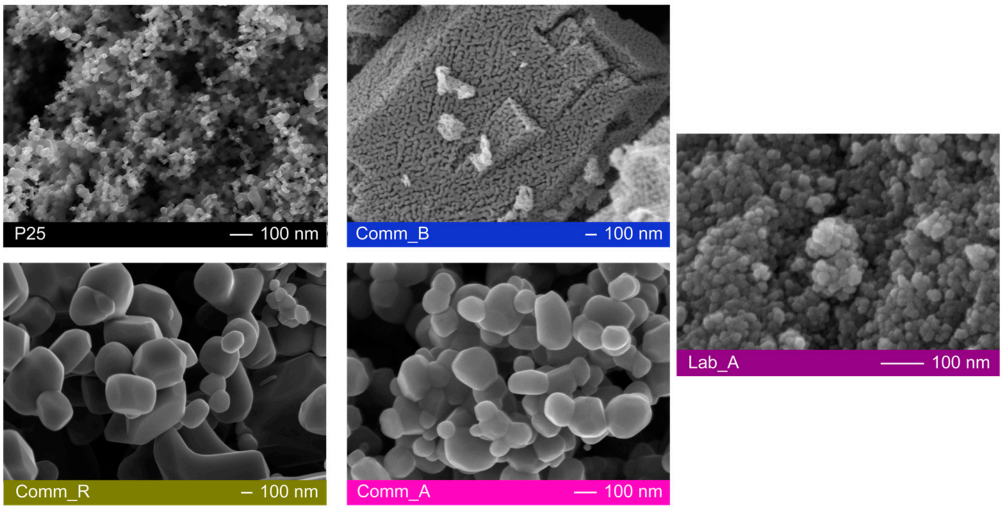

Figure 2. Selected FESEM micrographs of the studied powder samples, showing particles with different sizes, morphology, and agglomeration/aggregation.

Figure 3a reports the N_2 adsorption/desorption isotherms at −196 °C. The four commercial powders show type II isotherms, typical of non-porous (or macroporous) adsorbents; at variance with both Comm_A and Comm_R, P25 shows a (limited) hysteresis loop (of the H3 type), typical of non-rigid aggregates, due to the presence of agglomerated/aggregated non-porous nanoparticles (*vide supra*), with N_2 condensation at a high relative pressure (i.e., $P/P^0 > 0.85$), due to the presence of some inter-particle meso/macropores [38,39] and, accordingly a higher SSA as compared to Comm_A and Comm_R. The Comm_B sample shows a pronounced H1 hysteresis loop, typical of cylindrical pores, which may be due to nanoparticle aggregation/agglomeration, leading to the formation of inter-particle pores, as observed by FESEM (Figure 2). The Lab_A sample shows a type IV isotherm, with a pronounced H2 type hysteresis loop, due to inkbottle inter-particle mesopores. A previously reported TEM study showed that the adopted synthesis procedure brings about the formation of some intra-particle mesopores, in addition to inter-particle ones [38,39]. The BET SSA values follow the order: Lab_A >> P25 > Comm_B > Comm_A > Comm_R. Higher SSA values may be due to the occurrence of mesopores, the size of which could affect reagents/products diffusion. The PSD (Pore Size Distribution) curves in Figure 3b show that the three samples at higher SSA (namely, Lab_A, P25, and Comm_B) have broad PSD and pores diameter exceeding the molecular size of paracetamol (ca. 1.0×0.25 nm [44]), indicating that the whole available surface area should be accessible to the reagent and its products (detailed in Scheme 2), not affecting the reaction kinetics.

The physicochemical characterization reported so far showed that the commercial powders have markedly different textural and morphological properties, which may affect their photocatalytic performance, along with their surface properties (surface charge, functional groups). Figure 4 reports the electrophoretic measurements on the studied powders; the measured ζ-potential values may indicate that the particles are not very stable in suspension and tend to aggregate/agglomerate, as stable suspensions are usually characterized by surface charge values above +30 mV and below −30 mV (dotted lines, [45]).

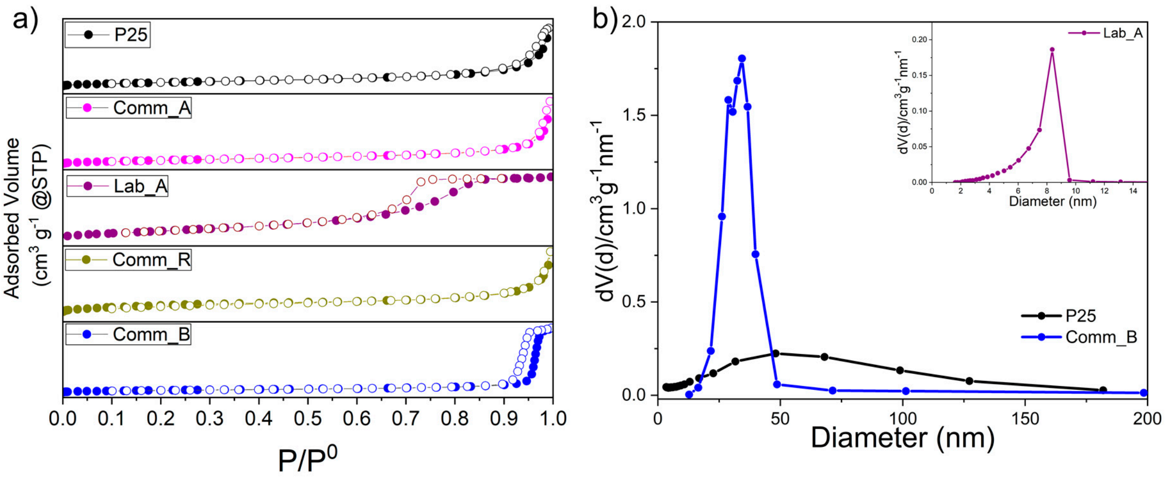

Figure 3. (**a**) N_2 adsorption/desorption isotherms at −196 °C on the studied powder samples.Full and empty symbols refer to adsorption and desorption run, respectively. (**b**) Pore Size Distribution of the P25, Comm_B, and Lab_A samples, as obtained by applying the BJH method to the isotherms desorption branch.

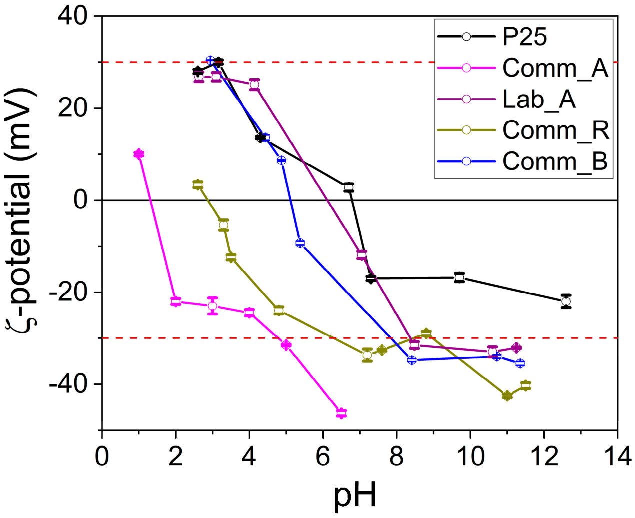

Figure 4. ζ-potential curves of the studied powders.

P25 has a value of pH at the isoelectric point (pH_{IEP}) equal to 6.77, in agreement with the literature, reporting for P25 values in the 6–7 pH range [45]. The Lab_A and the Comm_B powders have values of 6.07 and 5.11, respectively, in agreement with the literature, reporting that brookite has slightly stronger Brønsted sites as compared to anatase and rutile [46], leading to lower pH_{IEP} values (as compared to anatase and rutile).

Conversely, the Comm_A and Comm_R show markedly low pH_{IEP} values, which could be ascribed to the presence of surface impurities, finally altering their surface charge in water. The powders chemical composition was therefore studied using both EDX and XPS analyses (Table 1). EDX (semi-quantitative) elemental analysis revealed the occurrence of some K (0.16 at.%) and P (0.27 at.%) impurities with the Comm_A sample, likely due to residues of crystallization control agents (i.e., K_3PO_4) that can be added during the synthesis to obtain the anatase phase [42]; concerning the surface composition, the same elements were detected by XPS, at a higher concentration (2.9 at.% K, and 2.7 at.% P, respectively), confirming that the impurities are mostly located at the surface of Comm_A particles [47], as XPS allows surface chemical analysis, whereas EDX also probes the bulk, at least partially. Based on these results, the lower pH_{IEP} of the Comm_A sample can be ascribed to the not negligible presence of some K_3PO_4-deriving impurities at the sample surface, in agreement with the literature showing that phosphate-rich TiO_2 surfaces exhibit lower pH_{IEP} values [48] than “clean” TiO_2 surfaces. No impurities were detected by XPS at the surface of the Lab_A sample, which, accordingly, showed a pH_{IEP} value in agreement with literature values typical of a “clean” anatase surface.

Concerning the Comm_R powder, which showed a low pH_{IEP}, a previous systematic literature study [49] showed that rutile particles with extremely rough surfaces may suffer a reduction of several units of pH_{IEP} as compared to rutile particles with flat crystalline surfaces; however, XPS analysis detected the presence ca. 0.7 at. % Cl at the surface of Comm_R particles, and such surface impurities could contribute to the low pH_{IEP} value of the sample [50]. Concerning the Comm_B and P25 powders, EDX analysis probed the presence of some Cl species, but in a small amount (0.03 at. % in Comm_B and 0.09 at % in P25) and limitedly to some spots of the samples (the EDX data in Table 1 are, indeed, an average of at least four/five measurements in as many different spots). XPS did not detect impurities at the surface of P25 and of Comm_B, aside from naturally occurring adventitious carbon. Accordingly, the measured pH_{IEP} values agree with the literature values for brookite [46] and P25 [45], respectively.

The occurrence of surface impurities could also affect the overall photocatalytic performance, especially if phosphate species at the surface of Comm_A are concerned [48,51–53].

Concerning High-Resolution XP spectra, the curve-fitting procedure on the Ti 2p and O1s lines (not shown) led to the determination of the lines assigned to the surface species reported in Table 2, showing the occurrence of Ti^{4+} ions, and of some oxygen species expected at the surface of TiO_2, namely lattice O^{2-}, surface OH groups and O species due to adsorbed H_2O and/or C-containing compounds [54,55]. The Ti 2p spectral region showed the typical spin-orbit splitting doublet of Ti $2p_{3/2}$ and Ti $2p_{1/2}$ species (Table 2). The observed splitting between the two Ti 2p lines is constant and equal to 5.7, confirming the sole presence of surface Ti^{4+} species [56]. The line at 532.44 eV observed with Comm_A could be due to the presence of phosphate-related oxygen atoms; correspondingly, with the same sample, an additional line was observed at 292.5 eV, a BE typical of K^+ in K_3PO_4 [57,58] and therefore ascribed to the K 2p line.

Table 2. Results of XPS analysis concerning the surface chemical composition and the curve-fitting of the Ti 2p and O1s lines; band-gap values, as obtained from DR-UV-Vis spectra by applying the Tauc’s plot method and by extrapolation of the absorption onset; VB value as obtained by XPS analysis and calculated CB energy.

Sample	O 1s BE (eV)		Ti 2p$_{1/2}$/ Ti 2p$_{3/2}$ BE (eV)		Tauc’s Plot Determined/Onset Extrapolated E_g (eV)	XPS Determined VB Energy (eV)	CB Energy (eV)
Comm_A	Lattice O^{2-}	529.52	Ti^{4+}	464.06/ 458.36	3.30/3.28	2.54	5.83
	OH^-	530.47					
	Phosphate O	532.44					
Comm_R	Lattice O^{2-}	529.77	Ti^{4+}	464.27/ 458.57	3.02/3.03	2.49	5.52
	OH^-	531.10					
P25	Lattice O^{2-}	529.70	Ti^{4+}	464.16/ 458.46	3.33/3.31	2.70	6.02
	OH^-	531.95					
	H_2O/organic	533.51					
Comm_B	Lattice O^{2-}	529.20	Ti^{4+}	463.66/ 457.94	3.30/3.32	2.40	5.36
	OH^-	530.20					
Lab_A	Lattice O^{2-}	529.78	Ti^{4+}	464.28/ 458.58	3.20/3.18	2.58	5.78
	OH^-	531.08					

Figure 5a reports the Diffuse Reflectance (DR) UV-Vis spectra of the studied powders. As expected, all the UV-Vis spectra are dominated by a strong absorption in the UV range, due to charge transfer transition from O^{2-} to Ti^{4+} ions. P25 (absorption onset at λ = 373 nm) and Comm_B (onset at λ = 368 nm) absorb in slightly narrower range as compared to Comm_A (onset at λ = 378 nm), Lab_A (onset at λ = 388 nm) and Comm_R (onset at λ = 406 nm). Figure 5b compares the corresponding Tauc’s plots, as obtained by assuming direct transition ($(F(R)*h\nu)^2$) with both Comm_R (95.0 % rutile, direct semi-conductor) and Comm_B (100% brookite, direct semi-conductor) and indirect transition ($(F(R)* h\nu)^{1/2}$)

with Lab_A (100 %anatase, indirect semi-conductor), Comm_A (97.7 % anatase, indirect semi-conductor) and P25 (88 %anatase). Table 2 compares the corresponding bandgap values (E_g, eV) as calculated from the onset of absorption (E_g, = 1240/λ) and by applying Tauc's plot method, showing a good agreement between the two sets of values.

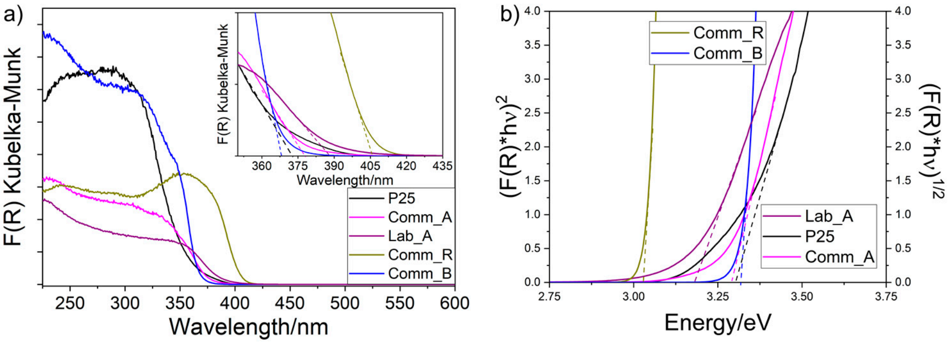

Figure 5. (**a**) DR UV-Vis spectra of the studied powders, where dotted lines allow determination of the bandgap energy from the onset of absorption. (**b**) The Corresponding Tauc's plot, as obtained by considering Comm_B and Comm_R as direct semiconductors, and Comm_A, Lab_A, and P25 as indirect semiconductors, and where dotted lines allow determination of the bandgap energy from the plot.

By considering the mathematical average of the two bandgap values calculated for each sample and the VB (valence band) energy, as obtained by XPS, the CB (conduction band) energy values have been calculated and reported in Table 2. The values show that the studied powders differ not only in terms of type(s) of polymorph(s), NPs size/morphology, surface area, porosity, and light absorption properties but also in terms of surface composition, which could, in turn, affect the photocatalytic properties, at least for the anatase sample, as phosphate ions are recognized to have a prominent role in the photocatalytic properties of TiO_2 [51,52].

2.2. Photocatalytic Degradation of Paracetamol under 1 SUN

Figure 6 reports the spectra concerning the experiments of paracetamol degradation in the presence of 1 g L^{-1} photocatalyst, as obtained with the four commercial samples and with the Lab_A sample. The dotted curve is the UV-Vis spectrum of the starting paracetamol solution. As reported in the literature, the UV-Vis spectrum of paracetamol in water (dotted line) shows two bands at 194 and 243 nm, due to the $\pi \rightarrow \pi^*$ and to the $n \rightarrow \pi^*$ electronic transitions of the aromatic ring and the C=O group, respectively [59]. A blank test was carried out in the same conditions, but in the absence of any photocatalyst, showing, as expected, the near nihil contribution of solar photolysis to paracetamol degradation (Figure S1).

Before illumination with 1 SUN, in each experiment, the solution was left equilibrating with the powders for 1 h in dark conditions and without altering the pH. At the natural pH of the solution (pH = 5.7), the paracetamol molecule is neutral (pK_a = 9.5), being negatively charged at pH > 9.5 due to deprotonation of the phenolic group (Scheme 1). No relevant adsorption of paracetamol was observed, as the spectrum intensity in dark conditions (not shown) did not vary appreciably with the studied powders, indicating that the molecule does not strongly interact with the samples surface. This is an important finding that affects both the kinetic order of the reaction and the effect of surface impurities, especially with the Comm_A powder, as discussed later.

Figure 6 shows that, except for Comm_R, in the adopted reaction conditions all the photocatalysts led to (almost) complete degradation of paracetamol, as both the 194 and 243 nm bands are nearly absent after 5 h irradiation, indicating that the powders can efficiently exploit the UV fraction of the solar spectrum. Concerning paracetamol degradation, according to the literature, aromatic by-products form at the beginning of the photocatalytic degradation, and the final products are carboxylic acids [59–61]. Concerning the plausible degradation mechanism(s) of paracetamol, two of them are acknowledged in the literature [59,62], and are summarized in Scheme 2. The Scheme shows that the two most common pathways involve either elimination of the -NH-CO-CH_3 group, followed by the formation of hydroquinone and 1,2,4-trihydroxybenzene and carboxylic acids (pathway a), or elimination of the CO-CH_3 group, followed by the formation of 4-aminophenol and 4-nitrophenol, before the formation of hydroquinone and 1,2,4-trihydroxybenzene and carboxylic acids (pathway b) [59]. According to the literature, pathway a is slower and less probable than pathway b [62].

In Figure 6, while paracetamol bands decrease, additional bands form and then disappear, indicating the occurrence of different by-products that are, in turn, degraded to a different extent, i.e., poorly by Comm_R, which was the least active powder, but very efficiently by the other powders, leading to the formation of carboxylic acids, which are the final products expected from paracetamol degradation, whatever its degradation mechanism (Scheme 2). More specifically, with Comm_A, after 1 h reaction, the main bands of paracetamol are removed, with the formation of by-products characterized by bands at 215, 290, and 315 nm, which are, in turn, degraded in the next hour, when a new band forms at 205 nm, and finally residual products absorb at 195 nm. The band at 215 nm can be due to the formation of 1,2,4-trihydroxybenzene, forming by loss of the NH-CO-CH_3 group (pathway b in Scheme 2) and oxidation by photogenerated hydroxyls radical, whereas the bands at 290 and 315 nm can be due to the formation of hydroquinone and 4-nitrophenol, respectively [59]. At a longer time, the band occurring at 205 nm can be due to carboxylic acids, which are then degraded, and the band at 195 nm to residual acetamide molecules deriving from the elimination of the NH-CO-CH_3 group. Comm_B, P25, and Lab_A seem to follow the pathway b, but with Comm_B (similar to Comm_A) no residual band was present at 290 nm after 5 h, suggesting the presence of carboxylic acids, only.

With Comm_R, a slower paracetamol degradation was observed (pathway a in Scheme 2 [62]) in that after the formation of hydroquinone and 1,2,4-trihydroxybenzene the carboxylic acids band was not observable.

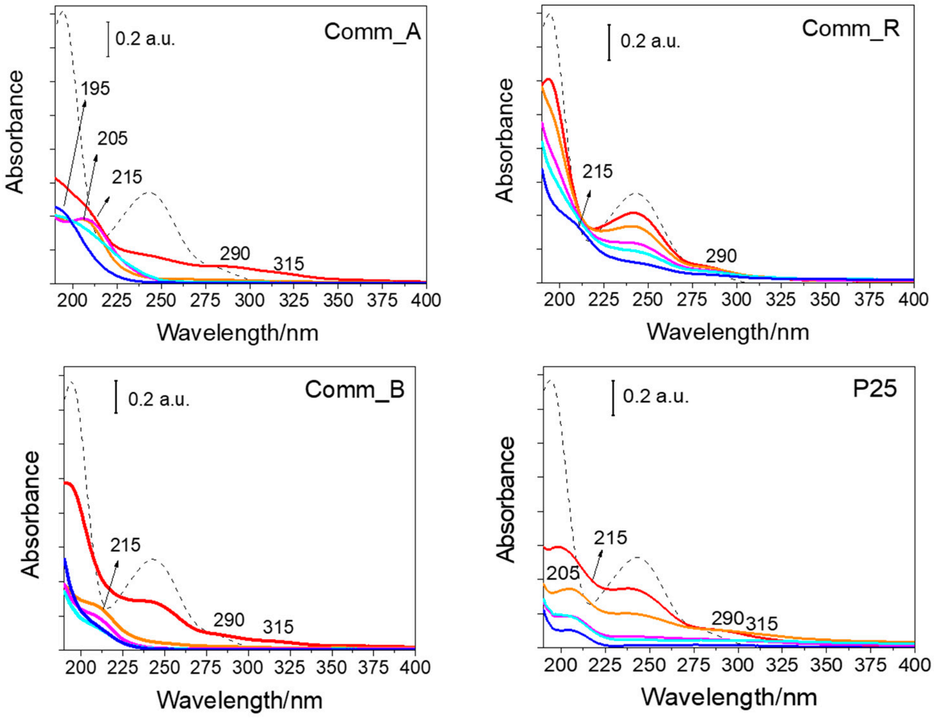

Figure 6. *Cont.*

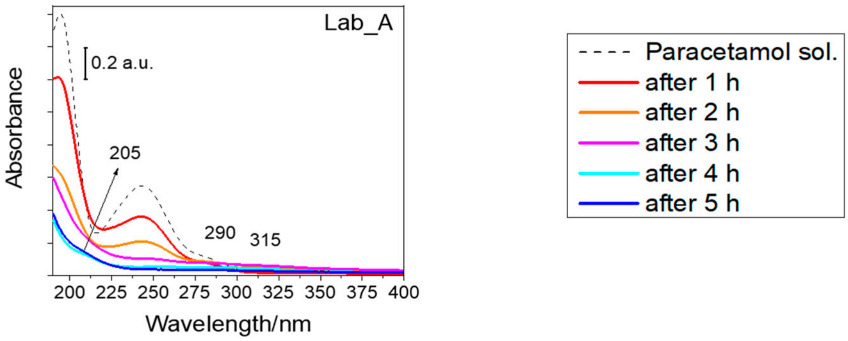

Figure 6. UV-Vis spectra of the starting 0.01 mM paracetamol solution and of the supernatant aliquots withdrawn after 1, 2, 3, 4, and 5 h solar illumination with the following samples: Comm_A, Comm_R, Comm_B, P25, and Lab_A. The photocatalyst concentration was 1.0 g L^{-1}. The written wavelengths indicate some bands due to the formation of possible by-products based on Scheme 2.

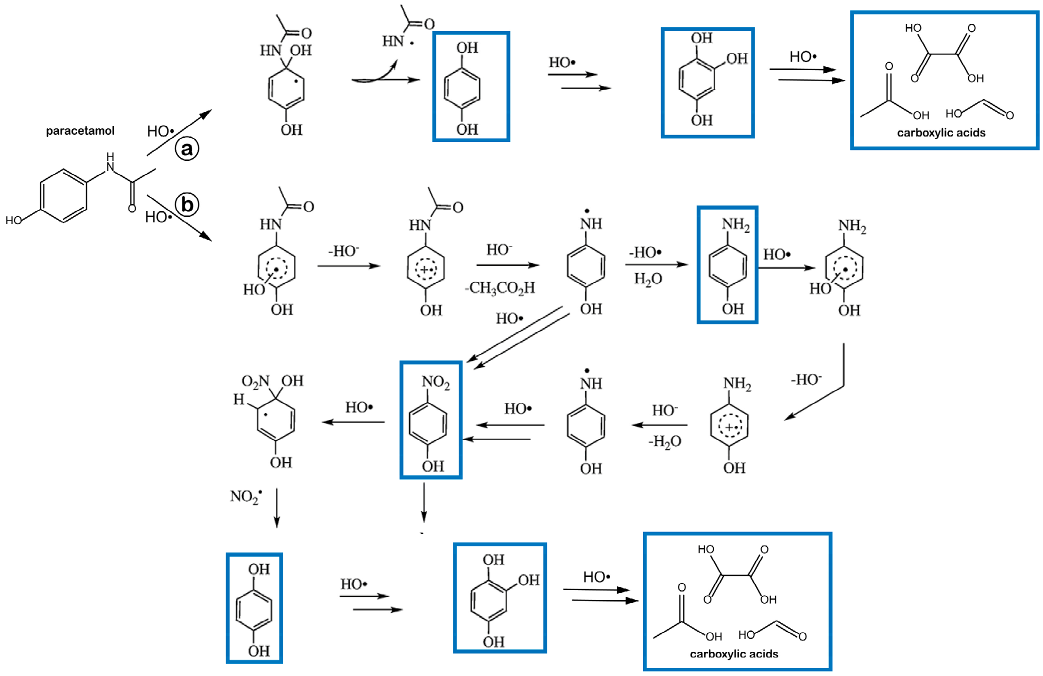

Scheme 2. Paracetamol degradation pathways according to the literature, adapted from refs. [59,62]. Compounds in the boxes correspond to possible by-products identified by UV-Vis spectroscopy and forming during the experiments in Figure 6.

Summarizing, except for Comm_R, all the powders were active toward the degradation of paracetamol, indicating a fair exploitation of the UV fraction of the solar spectrum, especially by Comm_A and Comm_B.

Formation of by-products and their simultaneous degradation along with that of (residual paracetamol molecules) did not allow us to carry out a more detailed kinetic study on the data obtained with 1 g L^{-1} photocatalyst, therefore another set of experiments was made at a lower photocatalyst concentration, namely 0.15 g L^{-1}. As expected, at a smaller photocatalyst concentration, the degradation of paracetamol occurred to a lower extent with the formation of some by-products that were, in turn, degraded, very efficiently with Comm_A and Comm_B, and less efficiently with the other samples. As expected, Comm_R was poorly active under solar illumination, due to its very low specific surface area and the fact that electron/hole recombination easily occurs, being a direct semiconductor [43]; however, the presence of surface impurities could have a role in the activity, and thus the powder was treated in O_2 atmosphere at 450 °C to remove the surface Cl species. The procedure led to partial removal of surface Cl species (the surface at % Cl decreased from

0.7 to 0.3, as determined by XPS analysis) with the oxidized sample, however, only a slight decrease of the intensity of the 194 nm band was observed (Figure S2), indicating the removal of some -CH_3-CO groups (pathway b in Scheme 2), but the same remained poorly active, indicating that surface Cl impurities marginally affect the (overall poor) Comm_R activity.

Figure 7 also reports the ln(C/C_0) (for Comm_A) and the C/C_0 trends with time (for the other four powders), as obtained by considering the intensities of the 243 nm band, to determine the kinetic constants reported in Table 3. Interestingly, with Comm_A a pseudo-first-order kinetic was observed, whereas, with the other powders, a pseudo-zero-order kinetic.

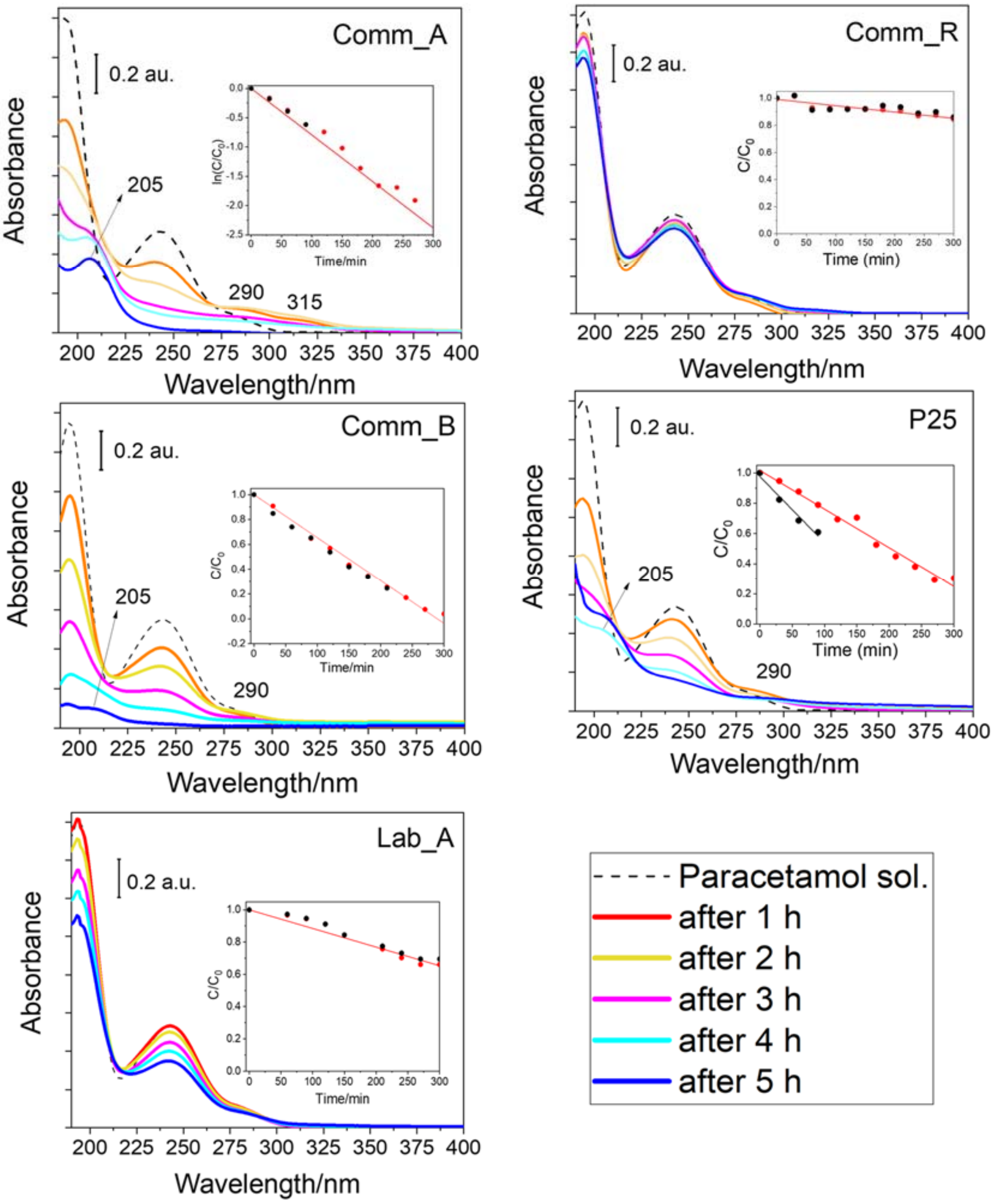

Figure 7. UV-Vis spectra of the starting 0.01 mM paracetamol solution and of the supernatant aliquots withdrawn after 1, 2, 3, 4, and 5 h solar illumination with the following samples: Comm_A, Comm_R, Comm_B, P25, and Lab_A. The photocatalyst concentration was 0.15 g L^{-1}. The insets refer to kinetics curves as obtained by following the 243 nm band intensity (red symbols) and the 194 nm band (black symbols).

Table 3. Observed reaction order; kinetic constant values as determined by considering the intensity of the 243 nm band (k_{243}); total paracetamol conversion as determined by considering the intensity of the 243 nm band after 300 min during the photocatalytic tests with 0.15 g L^{-1} powder in 0.01 mM paracetamol solution.

Photocatalyst	Observed Reaction Order	Kinetic Constant (k_{243}) Value	Paracetamol % Conversion after 300 min
Comm_A	1	7.2×10^{-3} mol L^{-1} min^{-1}	95 %
Lab_A	0	1.2×10^{-3} min^{-1}	34 %
Comm_R	0	5.1×10^{-4} min^{-1}	15 %
Comm_B	0	3.5×10^{-3} min^{-1}	96 %
P25	0	2.5×10^{-3} min^{-1}	63 %

In the literature, a pseudo-first-order kinetic is usually obtained for the photodegradation of paracetamol. Most papers, however, report results obtained in markedly different conditions, i.e., under UV illumination, at different starting pH and/or by bubbling $O_{2(g)}$ and, therefore, careful comparison with those data is not straightforward [59,60]. The pseudo-zero-order kinetics observed in this work with all the studied samples, except Comm_A, is compatible with the limited supply of oxygen to the reaction, which is one of the possible reasons for zero-order kinetic processes [63]. With the Comm_A sample, a pseudo-first-order kinetic was observed, which can be ascribed to the different surface charge of the sample at the natural pH of the paracetamol solution (i.e., 5.7). Indeed, Lab_A, P25, and Comm_B are near to their pH_{IEP}, whereas the surface of Comm_A is negatively charged, thus can interact more strongly with some positively charged portion of the paracetamol molecule, although this does not lead to strong adsorption processes during the dark part of the experiments (*vide supra*).

Table 3 also reports the overall percentage of degraded paracetamol, as determined by considering the intensity of the 243 nm band, showing that both Comm_A and Comm_B outperform P25. Concerning Comm_B, this behavior may be due to the nanometric size of its particles, whereas concerning Comm_A there is very likely a prominent role of the surface impurities.

Concerning the evaluation of the parameters in Table 3 by following the 243 nm band, i.e., as usually made in the literature [59], one may object that the formation of by-products characterized by UV bands around 243 nm may affect the calculation with other types of contaminants [64,65]. Other authors have been able to determine the actual contribution of the bands of the contaminant (phenol) and the by-products through a careful curve-fit procedure, not possible with the broad bands observed in our UV-Vis spectra. Therefore, to confirm the values in Table 3, we reported as black dots the intensities of the other paracetamol band at 194 nm in the conditions when the formation of by-products did not perturb its position, except for P25, the 194 nm band symbols are fairly superposed to those of the 243 nm band, confirming that at least under these adopted conditions (type of reactor and photocatalyst, paracetamol concentration, etc.) the values in Table 3 are reliable. With P25, k_{243} is in fair agreement with the literature values [66]; the slope of the line obtained from the intensity of the 194 nm band was higher (i.ee., 5.79×10^{-3} min^{-1}), but with Comm_A and Comm_B only the bands of carboxylic acids were observed after 5 h reaction, confirming that the two powders outperformed P25.

2.3. About the Remarkable Photocatalytic Activity of the Comm_A and the Comm_B Powders

As compared to the Lab_A sample, the Comm_A sample is characterized by a lower SSA, a larger E_g value larger and sub-micrometric particles, i.e., by a set of physicochemical properties that should worsen its photocatalytic performance. To confirm that this behavior is likely due to the occurrence of surface phosphate species, two additional experiments were made. The Comm_A powder recovered after 5 h (Recycled Comm_A) was contacted with a fresh paracetamol solution; in the latter, an aliquot of the Lab_A sample was impregnated with an aqueous solution of K_3PO_4 (the compound used as crystallization agent of commercial anatase) and the resulting powder (Lab_A_imp) was contacted with a fresh paracetamol solution. Impregnation with K_3PO_4 did not alter the phase composition, mesoporosity, and morphology of the Lab_A_imp, but led to a slight decrease in the SSA as compared to the parent sample (Figures S3 and S4).

Figure 8 reports the comparison of the spectra of the supernatant solutions obtained after a 1 h reaction with the Comm_A, the Recycled Comm_A, the Lab_A, and the Lab_A_imp powders. Interestingly, the Recycled Comm_A was less active than the Comm_A, and, accordingly, the residual surface P concentration was 0.9%, as measured by XPS analysis. The Lab_A_imp sample was more active than the Lab_A sample, notwithstanding the low P content (0.5 at % as determined by XPS) and the decrease of the SSA as compared to the parent powder. Moreover, with the Lab_A_imp sample a pseudo-first-order kinetic was observed (Figure S5), similar to the Comm_A powder, and the sample was more active than the parent powder, at least in the first 2 h of the reaction.

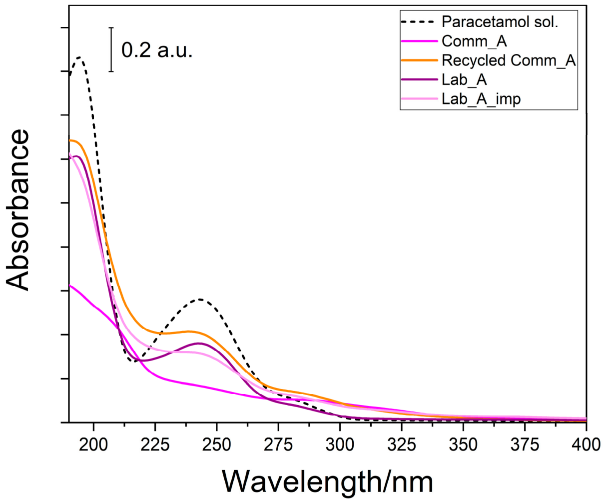

Figure 8. Comparison of the UV-vis spectra (190–400 nm range) of the supernatant solutions taken after 1 h reaction under 1 SUN with 1 g L^{-1} of Comm_A, Recycled Comm_A, Lab_A, and Lab_A_imp powders in the presence of 0.01 mM paracetamol solution.

It has been reported that anatase and brookite are capable of both O_2 reduction to $HO_2\cdot$ and H_2O oxidation to $HO_2\cdot$ [67]. On the other hand, Scheme 3 reports computational values (E_{vac}) of the valence and conduction band (VB, CB) energy of the three polymorphs of TiO_2 [68] addressed in this paper (namely, brookite, anatase, and rutile) and of the paracetamol molecule HOMO (highest occupied molecular orbital) and LUMO (lowest unoccupied molecular orbital) levels [69]. Based on such computational values, the position of the VB of the three polymorphs can help direct the oxidation of paracetamol by photogenerated h^+_{VB}, especially by brookite, having the closest VB to the paracetamol's HUMO. In the present case, however, no adsorption was observed, and the direct oxidation process seems unlikely.

Concerning the Comm_A sample, it has to be remarked that the positive effect of surface phosphate ions on the photocatalytic activity of anatase has been already documented by the literature [52] reporting that TiO_2 surface modification by phosphate affects the photocatalytic degradation of some contaminants, in terms of both rates and pathways of degradation; specifically, adsorbed phosphate ions improve the photocatalytic degradation of substrates weakly interacting with the surface, akin to the present case, where no adsorption of paracetamol has been observed, whereas the effect is opposite, if the interaction is stronger, i.e., phosphate ions can decrease the photocatalytic activity of TiO_2. According to the literature, surface phosphate ions largely accelerate the hydroxyl radicals attack, hindering, instead, the direct hole oxidation pathway (Scheme 3). Furthermore, the negatively charged surface ions are responsible for the lower pH_{IEP} [52], but also give rise to a negative electrostatic field that promotes the separation between the charge carriers and hampers their recombination as compared to a "clean" TiO_2 surface.

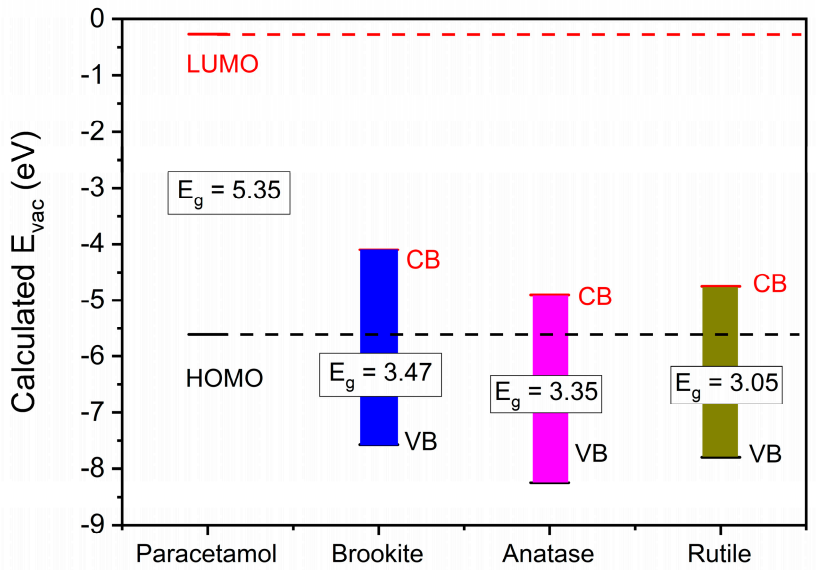

Scheme 3. Calculated VB and CB values of brookite, anatase, and rutile TiO_2 polymorphs and calculated HOMO and LUMO values of paracetamol [56].

Concerning the remarkable photocatalytic activity of the Comm_B sample, on the one hand, Scheme 3 shows the favorable band alignment with the HOMO and LUMO levels of the paracetamol molecule, which could favor the direct oxidation of paracetamol by photogenerated h^+_{VB}; on the other hand, no adsorption phenomena were observed in our experimental conditions. Therefore, we are inclined to ascribe the very good photocatalytic performance of the Comm_B powder to a combination of its physicochemical properties, i.e., the particle nanometric size and the peculiar (i.e, moderate) depth of brookite electron trapping states, which, according to the literature, can reduce the recombination of photogenerated e^-_{CB}, and h^+_{VB} [70]. The results obtained with the Comm_B sample are indeed in agreement with the previous literature reports on the efficient photocatalytic degradation of other environmental pollutants by nanometric brookite samples [71,72].

3. Materials and Methods

The following commercial powders were studied: Aeroxide® TiO_2 P25 (P25, purity $\geq$ 99.50 %, Evonik, Frankfurt, Germany); an anatase powder (Comm_A, 99.8 % purity based on trace metal analysis, metal traces $\leq$ 2500.0 ppm, CAS number 1317-70-0, Merck-Sigma-Aldrich, Schnelldorf Distribution); a rutile powder (Comm_R, purity $\geq$ 99.9 %, based on trace metal analysis, metal traces $\leq$ 1000.0 ppm, CAS number 1317-80-2, Merck-Sigma-Aldrich, Schnelldorf Distribution) and a brookite powder (Comm_B, nanopowder, purity = 99.99 %, metal traces $\leq$ 150.0 ppm, CAS number 12188-41-9,Merck Sigma-Aldrich, Schnelldorf Distribution).

A sample of mesoporous pure anatase according to a micelle template assisted sol-gel procedure detailed in refs. [35,58] (Lab_A). Briefly, two solutions, A and B, were prepared: solution A was obtained by drop-wise adding 5.0 g $Ti(OC(CH_3)_3)_4$ (titanium(IV) tert-butoxide, 97%) to 30.0 mL acetic acid solution (20%, v/v) and vigorously stirring for about 4 h; solution B was obtained by mixing 3.0 g Pluronic P123 and ca. 20.0 mL ethanol. Solution B was, then, dropwise added to solution A and the resulting mixture was sealed, stirred for 24 h at room temperature, and transferred into a Teflon autoclave for hydrothermal treatment at 85 °C for 48 h. The resulting precipitate was centrifuged, dried at 80 °C, and calcined in air at 450 °C for 4 h.

An aliquot of the Lab_A powder was contacted with a 0.0 M K_3PO_4 aqueous solution for 5 h under stirring at 80 °C. The powder was then kept in the oven for 1 night at 80 °C and repeatedly washed with Milli-Q bidistilled water and finally dried at 80 °C.

An X'Pert Philips PW3040 diffractometer (Panalytical, Almelo, Netherland)using Cu Kα radiation (2θ range = 20–70°; step = 0.026° 2θ; time per step = 0.8 s) was used to collect X-ray powder diffraction (XRD) patterns, which were indexed with Powder Data File database (PDF 2000, International Centre of Diffraction Data, Pennsylvania). The X'Pert High Score Plus 3.0e software was used to obtain both Quantitative Phase Analysis (QPA) by applying the Rietveld method and the crystallite average size (D) through the Williamson-Hall plot.

FE-SEM (Field Emission Scanning Electron Microscopy) micrographs were taken on a Merlin FESEM instrument (Carl-Zeiss AG, Oberkochen, Germany) equipped with an EDX (Energy Dispersive X-ray Analysis) probe (Oxford instruments) for semi-quantitative elemental analysis. Typically, the sample composition has been analyzed by EDX in four/five spots of the samples and average values have been measured.

To calculate the Specific Surface Area (SSA) Brunauer-Emmett-Teller (BET) method was applied on N_2 adsorption/desorption isotherms measured at −196 °C (Micromeritics ASAP 2020Plus, Micromeritics, Norcross, GA, USA) on powders pre-outgassed at 150 °C for 4 h to remove atmospheric contaminants and water. A Cary 5000 UV-Vis-NIR spectrophotometer (Varian instruments) equipped with a Diffuse Reflectance (DR) sphere was used to acquire DR UV-vis spectra of powder samples.

A dynamic light scattering (DLS) Zetasizer Nano-ZS (Malvern Instruments, Worcestershire, UK) was used to obtain ζ-potential curves by measuring their electrophoretic mobility as a function of pH through the addition of either 0.1 M NaOH or 0.1 M HCl solutions. The powders were suspended in ultrapure water and then, sonicated for 2 min (10 W/mL, 20 kHz, Sonoplus, Bandelin, Berlin, Germany) and magnetically stirred for 5 min before each measurement.

X-Ray Photoelectron Spectroscopy (XPS) has been performed on a PHI 5000 VersaProbe (ULVAC-PHI, Physical Electronics Inc., Kanagawa, Japan) instrument, equipped with monochromatic Al Kα radiation (1486.6 eV energy) as an X-ray source. Two different pass energy values have been used for the survey (187.75 eV) and the HR spectra (23.5 eV). During the measurements, the charge compensation has been obtained with a combination of electron beam and low-energy Ar beam system.

All the photocatalytic tests were carried out by adding a proper amount of photocatalyst (corresponding to either 1.0 g L^{-1} or 0.15 g L^{-1} concentration) to 50 mL of 0.01 mM aqueous solution of paracetamol (natural pH = 5.7). Simulated solar light (AM 1.5 G, 100 mW cm^{-2}) was obtained by a plasma lamp (LIFI STA-40, LUXIM, Santa Clara, CA, USA). The illumination conditions were as follows: 1 SUN, i.e., ~1000 W m^{-2} in the visible range and ~22 W m^{-2} in the UV range. During the tests, the liquid/solid suspension inside the testing tube has been continuously stirred by a magnetic stirrer at ca. 300 rpm, as reported elsewhere [40]. The reaction mixture was not de-aerated although the reacting tube was sealed, with the consequence that the atmospheric O_2 was always present. At constant time intervals, aliquots of the suspension were withdrawn and immediately centrifugated at 12,000 rpm for 12 min (Thermo Fisher Scientific SL 16R centrifuge, Thermo Electron LED GmbH, Osterode am Harz, Germany) to obtain the supernatant solution, which was analyzed on UV-Vis-NIR spectrophotometer (Cary 5000, Varian Instruments, Mulgrave, Australia) to get UV-Vis spectra in the 190–800 nm range. With (more volatile) P25, the supernatant has been re-centrifuged at 12,000 rpm for 12 min and then, separated from the powder.

4. Conclusions

A commercial sub-micrometric powder of anatase, with a low specific surface area, was very active towards the photocatalytic degradation of paracetamol under simulated sunlight, likely due to the presence of surface residues of K_3PO_4, a common crystallization agent. As measured in the same conditions, the powder was more active than P25, the anatase/rutile mixture adopted as a benchmark in most of the literature studies, especially toward the degradation of paracetamol by-products. The commercial anatase powder was also more active than a nanometric anatase sample obtained by a lab synthesis procedure, with a clean surface and characterized by physicochemical properties that should lead to a higher activity as compared to the commercial anatase powder, namely a higher specific surface area, a smaller bandgap and smaller particles. Moreover, the lab-synthesized powder resulted to be more effective when modified with K_3PO_4, confirming our hypothesis, and agreeing with the previous literature studies on the subject. Concerning the rutile powder, the presence of surface chlorine did not affect appreciably its poor photocatalytic activity.

A nanometric brookite powder resulted to have a remarkable photocatalytic activity, in terms of paracetamol degradation, despite its broader energy gap and its low specific surface area, likely due to a combination of its physicochemical properties, namely the nanometric particles size and the peculiar (moderate) depth of its electron trapping states, in agreement with previous the literature reports on the degradation of other environmental pollutants. The studied commercial powders have been characterized by a multi-technique approach, to be able to relate their textural and surface properties to their photocatalytic activity, to find those properties affecting the overall photocatalytic performance and that could be developed by engineering new photocatalysts, possibly able to overcome the limitations of commercial ones.

Supplementary Materials: The following supporting information can be downloaded at: https://www.mdpi.com/article/10.3390/catal13020434/s1, Figure S1. UV-Vis spectra of the starting 0.01 mM paracetamol solution and of the supernatant aliquots withdrawn after 1, 2, 3, 4, and 5 h under solar illumination without any photocatalyst.; Figure S2. Trends of the C/C^0 values as obtained from the UV-Vis spectra of the starting 0.01 mM paracetamol solution (C^0) and of the supernatant aliquots withdrawn at regular time intervals under solar illumination in the presence of the oxidized Comm_R sample; Figure S3. (a) XRD patterns of the Lab_A_imp sample, showing only the peaks of the anatase phase (A); (b) N_2 adsorption/desorption isotherms at −196 °C of the Lab_A_imp sample, showing type IV isotherm, with a pronounced H2 type hysteresis loop, due to inkbottle inter-particle mesopores and a BET SSA = 105 $m^2\ g^{-1}$; Figure S4. Selected FESEM micrograph of the Lab_A_imp sample, showing the same morphology of the parent Lab_A sample; Figure S5. Trends of the C/C_0 values as obtained from the UV-Vis spectra of the starting 0.01 mM paracetamol solution (C_0) and of the supernatant aliquots withdrawn at regular time intervals under solar illumination in the presence of 1 g L^{-1} Lab_A_imp powder.

Author Contributions: Conceptualization, B.B. and F.S.F.; methodology, B.B.; formal analysis, data curation: N.B., S.G. and M.C.C.; investigation, N.D.; data curation, N.B., F.S.F., M.C.C. and N.D.; writing—original draft preparation, N.B.; writing—review and editing, B.B. and F.S.F.; supervision: B.B. and F.S.F. All authors have read and agreed to the published version of the manuscript.

Funding: The authors acknowledge the program PNRR Mac -2 NODES Nord Ovest Digitale e Sostenibile for funding this research.

Data Availability Statement: Not applicable.

Acknowledgments: The authors thank F. Deorsola (Department of Applied Science and Technology, Politecnico di Torino) for lending the anatase, rutile, and P25 commercial powders, S. Hernandez (Department of Applied Science and Technology, Politecnico di Torino) for lending the solar lamp, and T. Tosco (Department of Environment, Land and Infrastructure Engineering, Politecnico di Torino) for providing access to electrophoretic measurements.

Conflicts of Interest: The authors declare no conflict of interest.

References

1. Lee, T.H.Y.; Chuah, J.; Snyder, S.A. Occurrence of Emerging Contaminants in Southeast Asian Environments: Present Status, Challenges, and Future Prospects. *ACS ES&T Water* **2022**, *2*, 907–931. [CrossRef]
2. Wolfram, J.; Bub, S.; Petschick, L.L.; Schemmer, A.; Stehle, S.; Schulz, R. Pesticide occurrence in protected surface waters in nature conservation areas of Germany. *Sci. Total. Environ.* **2023**, *858*, 160074. [CrossRef] [PubMed]
3. Bexfield, L.M.; Toccalino, P.L.; Belitz, K.; Foreman, W.T.; Furlong, E.T. Hormones and Pharmaceuticals in Groundwater Used As a Source of Drinking Water Across the United States. *Environ. Sci. Technol.* **2019**, *53*, 2950–2960. [CrossRef] [PubMed]
4. Ferrario, C.; Finizio, A.; Villa, S. Legacy and emerging contaminants in meltwater of three Alpine glaciers. *Sci. Total. Environ.* **2017**, *574*, 350–357. [CrossRef] [PubMed]
5. Patel, M.; Kumar, R.; Kishor, K.; Mlsna, T.; Pittman, C.U., Jr.; Mohan, D. Pharmaceuticals of Emerging Concern in Aquatic Systems: Chemistry, Occurrence, Effects, and Removal Methods. *Chem. Rev.* **2019**, *119*, 3510–3673. [CrossRef] [PubMed]
6. Khasawneh, O.F.S.; Palaniandy, P. Occurrence and removal of pharmaceuticals in wastewater treatment plants. *Process. Saf. Environ. Prot.* **2021**, *150*, 532–556. [CrossRef]
7. Freyria, F.S.; Geobaldo, F.; Bonelli, B. Nanomaterials for the Abatement of Pharmaceuticals and Personal Care Products from Wastewater. *Appl. Sci.* **2018**, *8*, 170. [CrossRef]
8. Azcune, G.; Griffero, L.; Pareja, L.; Ríos, J.M.; Galbán-Malagón, C.; Pérez-Parada, A. Trends in the monitoring of legacy and emerging organic pollutants in protected areas. *Trends Environ. Anal. Chem.* **2022**, *34*, e00165. [CrossRef]
9. Boyd, G.R.; Reemtsma, H.; Grimm, D.A.; Mitra, S. Pharmaceuticals and personal care products (PPCPs) in surface and treated waters of Louisiana, USA and Ontario, Canada. *Sci. Total. Environ.* **2003**, *311*, 135–149. [CrossRef]
10. Yang, Y.; Zhang, X.; Jiang, J.; Han, J.; Li, W.; Li, X.; Yee Leung, K.M.; Snyder, S.A.; Alvarez, P.J.J. Which Micropollutants in Water Environments Deserve More Attention Globally? *Environ. Sci. Technol.* **2022**, *56*, 13–29. [CrossRef]
11. Freyria, F.S.; Sannino, F.; Bonelli, B. Common wastewater contaminants versus emerging ones: An Overview. *Nanomater. Detect. Remov. Wastewater Pollut.* **2020**, 19–46. [CrossRef]
12. Rodea-Palomares, I.; Gonzalez-Pleiter, M.; Gonzalo, S.; Rosal, R.; Leganes, F.; Sabater, S.; Casellas, M.; Muñoz-Carpena, R.; Fernández-Piñas, F. Hidden drivers of low-dose pharmaceutical pollutant mixtures revealed by the novel GSA-QHTS screening method. *Sci. Adv.* **2016**, *2*, e1601272. [CrossRef] [PubMed]
13. Luo, Y.L.; Guo, W.S.; Ngo, H.H.; Nghiem, L.D.; Hai, F.I.; Zhang, J.; Liang, S.; Wang, X.C. A review on the occurrence of micropollutants in the aquatic environment and their fate and removal during wastewater treatment. *Sci. Total Environ.* **2014**, *473–474*, 619–641. [CrossRef] [PubMed]
14. Li, M.; Yang, L.; Wu, X.; Chen, X.; Chen, F.; Zheng, X.; Song, Q.; Liu, X. Synergistic Removal of Nutrient Pollutants and Pharmaceutical and Personal Care Products (PPCPs) from Contaminated Groundwater: Macro- and Microelements and Microorganisms. *ACS ES T Water* **2022**, *2*, 1214–1224. [CrossRef]
15. Badmus, K.O.; Tijani, J.O.; Massima, E.; Petrik, L. Treatment of persistent organic pollutants in wastewater using hydrodynamic cavitation in synergy with advanced oxidation process. *Environ. Sci. Pollut. Res.* **2018**, *25*, 7299–7314. [CrossRef]
16. Tian, H.; Fan, Y.; Zhao, Y.; Liu, L. Elimination of ibuprofen and its relative photo-induced toxicity by mesoporous BiOBr under simulated solar light irradiation. *RSC Adv.* **2014**, *4*, 13061–13070. [CrossRef]
17. Philippe, K.K.; Timmers, R.; van Grieken, R.; Marugan, J. Photocatalytic Disinfection and Removal of Emerging Pollutants from Effluents of Biological Wastewater Treatments, Using a Newly Developed Large-Scale Solar Simulator. *Ind. Eng. Chem. Res.* **2016**, *55*, 2952–2958. [CrossRef]
18. Verlicchi, P.; Al Aukidy, M.; Zambello, E. Occurrence of pharmaceutical compounds in urban wastewater: Removal, mass load and environmental risk after a secondary treatment—A review. *Sci. Total Environ.* **2012**, *429*, 123–155. [CrossRef]
19. Ruan, T.; Field, J.; Cousins, I.; Lohmann, R.; Jiang, G. Emerging Contaminants: Fluorinated Alternatives to Existing PFAS. *Environ. Sci. Technol.* **2022**, *56*, 6001–6003. [CrossRef]
20. Ding, R.; Liu, S.; He, C.; Nie, X. Paracetamol affects the expression of detoxification- and reproduction-related genes and alters the life traits of Daphnia magna. *Ecotoxicology* **2020**, *29*, 398–406. [CrossRef]
21. Wilkinson, J.L.; Boxall, A.B.A.; Kolpin, D.W.; Leung, K.M.Y.; Lai, R.W.S.; Galbán-Malagón, C.; Adell, A.D.; Mondon, J.; Metian, M.; Marchant, R.A.; et al. Pharmaceutical pollution of the world's rivers. *Proc. Natl. Acad. Sci. USA* **2022**, *119*, e2113947119. [CrossRef] [PubMed]
22. Li, W.; Zhang, X.; Han, J. Formation of Larger Molecular Weight Disinfection Byproducts from Acetaminophen in Chlorine Disinfection. *Environ. Sci. Technol.* **2022**, *56*, 16929–16939. [CrossRef] [PubMed]
23. Reinstadler, V.; Ausweger, V.; Grabher, A.-L.; Kreidl, M.; Huber, S.; Grander, J.; Haslacher, S.; Singer, K.; Schlapp-Hackl, M.; Sorg, M.; et al. Monitoring drug consumption in Innsbruck during coronavirus disease 2019 (COVID-19) lockdown by wastewater analysis. *Sci. Total. Environ.* **2020**, *757*, 144006. [CrossRef] [PubMed]
24. Kolpin, D.W.; Furlong, E.T.; Meyer, M.T.; Thurman, E.M.; Zaugg, S.D.; Barber, L.B.; Buxton, H.T. Pharmaceuticals, Hormones, and Other Organic Wastewater Contaminants in U.S. Streams, 1999-2000: A National Reconnaissance. *Environ. Sci. Technol.* **2002**, *36*, 1202–1211. [CrossRef] [PubMed]
25. Togola, A.; Budzinski, H. Multi-residue analysis of pharmaceutical compounds in aqueous samples. *J. Chromatogr. A* **2008**, *1177*, 150–158. [CrossRef]

26. McNaught, A.D.; Wilkinson, A. Also Contains Definitions of: Heterogeneous Catalysis, Homogeneous. *IUPAC Compend. Chem. Terminol.* **2014**, *2291*, 2293. [CrossRef]
27. Chen, M.; Liu, J.; Bi, Y.; Rehman, S.; Dang, Z.; Wu, P. Multifunctional magnetic MgMn-oxide composite for efficient purification of Cd^{2+} and paracetamol pollution: Synergetic effect and stability. *J. Hazard. Mater.* **2020**, *388*, 122078. [CrossRef] [PubMed]
28. Wei, X.; Zhang, Q.; Cao, S.; Xu, X.; Chen, Y.; Liu, L.; Yang, R.; Chen, J.; Lv, B. Removal of pharmaceuticals and personal care products (PPCPs) and environmental estrogens (EEs) from water using positively charged hollow fiber nanofiltration membrane. *Environ. Sci. Pollut. Res.* **2020**, *28*, 8486–8497. [CrossRef]
29. Muqeet, M.; Gadhi, T.A.; Mahar, R.B.; Bonelli, B. Advanced nanomaterials for ultrafiltration membranes application. *Nanomater. Detect. Remov. Wastewater Pollut.* **2020**, 145–160. [CrossRef]
30. Rossetti, I.; Compagnoni, M.; Ramis, G.; Freyria, F.; Armandi, M.; Bonelli, B. Development of Unconventional Photocatalytic Reactors and Processes for the Abatement of Harmful N-Containing Pollutants. *Chem. Eng. Trans.* **2017**, *57*, 1663. [CrossRef]
31. Freyria, F.S.; Armandi, M.; Compagnoni, M.; Ramis, G.; Rossetti, I.; Bonelli, B. Catalytic and Photocatalytic Processes for the Abatement of N-Containing Pollutants from Wastewater. Part 2: Organic Pollutants. *J. Nanosci. Nanotechnol.* **2017**, *17*, 3654–3672. [CrossRef]
32. Compagnoni, M.; Ramis, G.; Freyria, F.S.; Armandi, M.; Bonelli, B.; Rossetti, I. Photocatalytic Processes for the Abatement of N-Containing Pollutants from Wastewater. Part 1: Inorganic Pollutants. *J. Nanosci. Nanotechnol.* **2017**, *17*, 3632–3653. [CrossRef]
33. Hernández-Leal, L.; Temmink, H.; Zeeman, G.; Buisman, C. Removal of micropollutants from aerobically treated grey water via ozone and activated carbon. *Water Res.* **2011**, *45*, 2887–2896. [CrossRef] [PubMed]
34. Gadhi, T.A.; Mahar, R.B.; Bonelli, B. Actual mineralization versus partial degradation of wastewater contaminants. *Nanomater. Detect. Remov. Wastewater Pollut.* **2020**, 331–350. [CrossRef]
35. Shahid, M.; Farooqi, Z.H.; Begum, R.; Arif, M.; Wu, W.; Irfan, A. Critical Reviews in Analytical Chemistry Hybrid Microgels for Catalytic and Photocatalytic Removal of Nitroarenes and Organic Dyes From Aqueous Medium: A Review) Hybrid Microgels for Catalytic and Photocatalytic Removal of Nitroarenes and Organic Dyes From Aqueous Medium: A Review. *Crit. Rev. Anal. Chem.* **2019**, *50*, 513–537. [CrossRef]
36. Ohno, T.; Sarukawa, K.; Tokieda, K.; Matsumura, M. Morphology of a TiO_2 Photocatalyst (Degussa, P-25) Consisting of Anatase and Rutile Crystalline Phases. *J. Catal.* **2001**, *203*, 82–86. [CrossRef]
37. Jiang, X.; Manawan, M.; Feng, T.; Qian, R.; Zhao, T.; Zhou, G.; Kong, F.; Wang, Q.; Dai, S.; Pan, J.H. Anatase and rutile in evonik aeroxide P25: Heterojunctioned or individual nanoparticles? *Catal. Today* **2017**, *300*, 12–17. [CrossRef]
38. Freyria, F.S.; Blangetti, N.; Esposito, S.; Nasi, R.; Armandi, M.; Annelio, V.; Bonelli, B. Effects of the Brookite Phase on the Properties of Different Nanostructured TiO_2 Phases Photocatalytically Active Towards the Degradation of N–Phenylurea. *Chemistryopen* **2020**, *9*, 903–912. [CrossRef]
39. Piumetti, M.; Freyria, F.S.; Armandi, M.; Geobaldo, F.; Garrone, E.; Bonelli, B. Fe- and V-doped mesoporous titania prepared by direct synthesis: Characterization and role in the oxidation of AO7 by H_2O_2 in the dark. *Catal. Today* **2014**, *227*, 71–79. [CrossRef]
40. Freyria, F.S.; Compagnoni, M.; Ditaranto, N.; Rossetti, I.; Piumetti, M.; Ramis, G.; Bonelli, B. Pure and Fe-Doped Mesoporous Titania Catalyse the Oxidation of Acid Orange 7 by H_2O_2 under Different Illumination Conditions: Fe Doping Improves Photocatalytic Activity under Simulated Solar Light. *Catalysts* **2017**, *7*, 213. [CrossRef]
41. Piumetti, M.; Freyria, F.S.; Armandi, M.; Saracco, G.; Garrone, E.; Gonzalez, G.E.; Bonelli, B. Catalytic degradation of Acid Orange 7 by H_2O_2 as promoted by either bare or V-loaded titania under UV light, in dark conditions, and after incubating the catalysts in ascorbic acid. *Catal. Struct. React.* **2015**, *1*, 183–191. [CrossRef]
42. Scientific Committee on Consumer Safety SCCS Opinion on Titanium Dioxide (TiO2) Used in Cosmetic Products That Lead to Ex-posure by Inhalation. 2020. Available online: https://health.ec.europa.eu/system/files/2021-11/sccs_o_238.pdf (accessed on 1 December 2022).
43. Manzoli, M.; Freyria, F.S.; Blangetti, N.; Bonelli, B. Brookite, a sometimes under evaluated TiO_2 polymorph. *RSC Adv.* **2022**, *12*, 3322–3334. [CrossRef]
44. Ahmed, L.O.; Omer, R.A. Journal of Physical Chemistry and Functional Materials Computational Study on Paracetamol Drug. *J. Phys. Chem. Funct. Mater.* **2020**, *3*, 9–13.
45. Holmberg, J.P.; Ahlberg, E.; Bergenholtz, J.; Hassellöv, M.; Abbas, Z. Surface charge and interfacial potential of titanium dioxide nanoparticles: Experimental and theoretical investigations. *J. Colloid Interface Sci.* **2013**, *407*, 168–176. [CrossRef] [PubMed]
46. Li, H.; Vrinat, M.; Berhault, G.; Li, D.; Nie, H.; Afanasiev, P. Hydrothermal synthesis and acidity characterization of TiO_2 polymorphs. *Mater. Res. Bull.* **2013**, *48*, 3374–3382. [CrossRef]
47. Kirstein, K.; Reichmann, K.; Preis, W.; Mitsche, S. Effect of commercial anatase-TiO_2 raw materials on the electrical characteristics of ceramics with positive temperature coefficient of resistivity. *J. Eur. Ceram. Soc.* **2011**, *31*, 2339–2349. [CrossRef]
48. Budarz, J.F.; Turolla, A.; Piasecki, A.F.; Bottero, J.-Y.; Antonelli, M.; Wiesner, M.R. Influence of Aqueous Inorganic Anions on the Reactivity of Nanoparticles in TiO_2 Photocatalysis. *Langmuir* **2017**, *33*, 2770–2779. [CrossRef]
49. Borghi, F.; Vyas, V.; Podestà, A.; Milani, P. Nanoscale Roughness and Morphology Affect the IsoElectric Point of Titania Surfaces. *PLoS ONE* **2013**, *8*, e68655. [CrossRef]
50. Cao, Z.; Zhang, T.; Ren, P.; Cao, D.; Lin, Y.; Wang, L.; Zhang, B.; Xiang, X. Doping of Chlorine from a Neoprene Adhesive Enhances Degradation Efficiency of Dyes by Structured TiO_2-Coated Photocatalytic Fabrics. *Catalysts* **2020**, *10*, 69. [CrossRef]

51. Hadjiivanov, K.I.; Klissurski, D.G.; Davydov, A.A. Study of phosphate-modified TiO_2 (anatase). *J. Catal.* **1989**, *116*, 498–505. [CrossRef]
52. Zhao, D.; Chen, C.; Wang, Y.; Ji, H.; Ma, W.; Zang, L.; Zhao, J. Surface Modification of TiO_2 by Phosphate: Effect on Photocatalytic Activity and Mechanism Implication. *J. Phys. Chem. C* **2008**, *112*, 5993–6001. [CrossRef]
53. Liu, X.; Chen, G.; Erwin, J.G.; Adam, N.K.; Su, C. Release of phosphorous impurity from TiO_2 anatase and rutile nanoparticles in aquatic environments and its implications. *Water Res.* **2013**, *47*, 6149–6156. [CrossRef] [PubMed]
54. Esposito, S.; Ditaranto, N.; Dell'Agli, G.; Nasi, R.; Rivolo, P.; Bonelli, B. Effective Inclusion of Sizable Amounts of Mo within TiO_2 Nanoparticles Can Be Obtained by Reverse Micelle Sol–Gel Synthesis. *ACS Omega* **2021**, *6*, 5379–5388. [CrossRef] [PubMed]
55. Bonelli, B.; Tammaro, O.; Martinovic, F.; Nasi, R.; Dell'Agli, G.; Rivolo, P.; Giorgis, F.; Ditaranto, N.; Deorsola, F.A.; Esposito, S. Reverse Micelle Strategy for the Synthesis of MnO_x–TiO_2 Active Catalysts for NH_3-Selective Catalytic Reduction of NO_x at Both Low Temperature and Low Mn Content. *ACS Omega* **2021**, *6*, 24562–24574. [CrossRef] [PubMed]
56. Nasi, R.; Esposito, S.; Freyria, F.S.; Armandi, M.; Gadhi, T.A.; Hernandez, S.; Rivolo, P.; Ditaranto, N.; Bonelli, B. Application of Reverse Micelle Sol–Gel Synthesis for Bulk Doping and Heteroatoms Surface Enrichment in Mo-Doped TiO_2 Nanoparticles. *Materials* **2019**, *12*, 937. [CrossRef] [PubMed]
57. Naumkin, A.v.; Kraut-Vass, A.; Gaarenstroom, S.W.; Powell, C.J. NIST X-Ray Photoelectron Spectroscopy Database. Available online: https://srdata.nist.gov/xps/Default.aspx (accessed on 1 December 2022).
58. X-Ray Photoelectron Spectroscopy (XPS) Reference Pages. Available online: https://srdata.nist.gov/xps/ (accessed on 1 December 2022).
59. Moctezuma, E.; Leyva, E.; Aguilar, C.A.; Luna, R.A.; Montalvo, C. Photocatalytic degradation of paracetamol: Intermediates and total reaction mechanism. *J. Hazard. Mater.* **2012**, *243*, 130–138. [CrossRef]
60. Yang, L.; Yu, L.; Ray, M.B. Photocatalytic Oxidation of Paracetamol: Dominant Reactants, Intermediates, and Reaction Mechanisms. *Environ. Sci. Technol.* **2008**, *43*, 460–465. [CrossRef]
61. Yang, L.; Bai, X.; Shi, J.; Du, X.; Xu, L.; Jin, P. Quasi-full-visible-light absorption by D35-TiO_2/g-C_3N_4 for synergistic persulfate activation towards efficient photodegradation of micropollutants. *Appl. Catal. B Environ.* **2019**, *256*, 117759. [CrossRef]
62. Vogna, D.; Marotta, R.; Napolitano, A.; D'Ischia, M. Advanced Oxidation Chemistry of Paracetamol. UV/H_2O_2-Induced Hydroxylation/Degradation Pathways and ^{15}N-Aided Inventory of Nitrogenous Breakdown Products. *J. Org. Chem.* **2002**, *67*, 6143–6151. [CrossRef]
63. Ollis, D.F. Kinetics of Photocatalyzed Reactions: Five Lessons Learned. *Front. Chem.* **2018**, *6*, 378. [CrossRef]
64. Su, R.; Tiruvalam, R.; He, Q.; Dimitratos, N.; Kesavan, L.; Hammond, C.; Lopez-Sanchez, J.A.; Bechstein, R.; Kiely, C.J.; Hutchings, G.J.; et al. Promotion of Phenol Photodecomposition over TiO_2 Using Au, Pd, and Au-Pd Nanoparticles. *ACS Nano* **2012**, *6*, 6284–6292. [CrossRef] [PubMed]
65. Mendoza-Damián, G.; Tzompantzi, F.; Pérez-Hernández, R.; Gómez, R.; Hernández-Gordillo, A. Photocatalytic properties of boehmite–SnO2 composites for the degradation of phenol. *Catal. Today* **2016**, *266*, 82–89. [CrossRef]
66. Trujillano, R.; Rives, V.; García, I. Photocatalytic Degradation of Paracetamol in Aqueous Medium Using TiO_2 Prepared by the Sol–Gel Method. *Molecules* **2022**, *27*, 2904. [CrossRef] [PubMed]
67. Li, Z.; Cong, S.; Xu, Y. Brookite vs Anatase TiO_2 in the Photocatalytic Activity for Organic Degradation in Water. *ACS Catal.* **2014**, *4*, 3273–3280. [CrossRef]
68. Buckeridge, J.; Butler, K.T.; Catlow, C.R.A.; Logsdail, A.J.; Scanlon, D.O.; Shevlin, S.A.; Woodley, S.M.; Sokol, A.A.; Walsh, A. Polymorph Engineering of TiO_2: Demonstrating How Absolute Reference Potentials Are Determined by Local Coordination. *Chem. Mater.* **2015**, *27*, 3844–3851. [CrossRef]
69. Hossen, M.B.; Siddique, Z.A.; Uzzaman, M.; Ahsan, A.; Chowdhury, K.U. A Computational Approach to Investigate the Biochemical Properties of Paracetamol and Its Metabolites. *Biomed. J. Sci. Tech. Res.* **2019**, *22*, 16860–16865. [CrossRef]
70. Vequizo, J.J.M.; Matsunaga, H.; Ishiku, T.; Kamimura, S.; Ohno, T.; Yamakata, A. Trapping-Induced Enhancement of Photocatalytic Activity on Brookite TiO_2 Powders: Comparison with Anatase and Rutile TiO_2 Powders. *ACS Catal.* **2017**, *7*, 2644–2651. [CrossRef]
71. Tran, H.T.T.; Kosslick, H.; Ibad, M.F.; Fischer, C.; Bentrup, U.; Vuong, T.H.; Nguyen, L.Q.; Schulz, A. Photocatalytic Performance of Highly Active Brookite in the Degradation of Hazardous Organic Compounds Compared to Anatase and Rutile. *Appl. Catal. B Environ.* **2017**, *200*, 647–658. [CrossRef]
72. Choi, M.; Lim, J.; Baek, M.; Choi, W.; Kim, W.; Yong, K. Investigating the Unrevealed Photocatalytic Activity and Stability of Nanostructured Brookite TiO_2 Film as an Environmental Photocatalyst. *ACS Appl. Mater. Interfaces* **2017**, *9*, 16252–16260. [CrossRef]